Journal of Power Sources 195 (2010) 4213–4221

Contents lists available at ScienceDirect

Journal of Power Sources

journal homepage: www.elsevier.com/locate/jpowsour

Effect of assembly error of bipolar plate on the contact pressure distribution and stress failure of membrane electrode assembly in proton exchange membrane fuel cell

Dong'an Liu, Linfa Peng, Xinmin Lai*

State Key Laboratory of Mechanical System and Vibration, Shanghai Jiao Tong University, Shanghai 200240, China

ARTICLE INFO

Article history:
Received 26 November 2009
Received in revised form
20 December 2009
Accepted 22 December 2009
Available online 14 January 2010

Keywords:
Assembly error
Metallic bipolar plate
Least squares-support vector machine
Error accumulation

ABSTRACT

In practice, the assembly error of the bipolar plate (BPP) in a PEM fuel cell stack is unavoidable based on the current assembly process. However its effect on the performance of the PEM fuel cell stack is not reported yet. In this study, a methodology based on FEA model, "least squares-support vector machine (LS-SVM)" simulation and statistical analysis is developed to investigate the effect of the assembly error of the BPP on the pressure distribution and stress failure of membrane electrode assembly (MEA). At first, a parameterized FEA model of a metallic BPP/MEA assembly is established. Then, the LS-SVM simulation process is conducted based on the FEA model, and datasets for the pressure distribution and Von Mises stress of MEA are obtained, respectively for each assembly error. At last, the effect of the assembly error is obtained by applying the statistical analysis to the LS-SVM results. A regression equation between the stress failure and the assembly error is also built, and the allowed maximum assembly error is calculated based on the equation. The methodology in this study is beneficial to understand the mechanism of the assembly error and can be applied to guide the assembly process for the PEM fuel cell stack.

1. Introduction

Fuel cells are considered to be promising alternative power devices due to their zero pollution and high efficiency [1]. Particularly, the proton exchange membrane (PEM) fuel cells have received broad attentions for automotive and portable applications because of their low-temperature operation, high power density and quick startup [2,3]. A typical PEM fuel cell stack is mainly composed of bipolar plate (BPP) housing the flow channels and membrane electrode assembly (MEA) [4]. The contact pressure distribution between the BPP and MEA is a key factor that influences the performance of PEM fuel cell. A high contact pressure can reduce the electrical resistance losses inside the cell. However, a large pressure may cause the gas diffusion layer (GDL) to be over compressed which results in the flow resistance increasing [5–8]. Furthermore, a large pressure may deform the MEA seriously causing its stress failure and internal short [9,10].

In practice, multiple single cells are usually connected in series to form a PEM fuel cell stack to provide the sufficient power and desired voltage as shown in Fig. 1. This configuration results in a high requirement of assembly accuracy for the adjacent BPPs. Otherwise, the assembly error will affect the perfect alignment of the adjacent BPPs and there will be an assembly position deviation d (Fig. 1), which leads to the assembly force F transmitting asymmetrically and in turn makes the contact pressure distribution between the BPP and MEA non-uniform. Moreover, such assembly error brings an extra moment M to the MEA, which may deform the MEA seriously and produce stress concentration (Fig. 1). According to [11–14], once the stress of MEA exceeds its yield strength, the plastic deformation will happen, and in turn, results in residual stresses in MEA after unloading, which are believed to be a significant contributor for the stress failure of MEA. Hence, it is very important to control the assembly error of the BPP to a low level in order to maintain a proper pressure distribution and avoid stress failure of the MEA.

However, the assembly error for the PEM fuel cell stack has not received enough attention currently, and in particular manual assembly processes are still widely applied for most of the stacks, which results in large assembly errors of the BPPs. Furthermore, during the running of a PEM fuel cell stack, the unavoidable vibration may aggravate the assembly error, especially for the automotive application due to more vibrations. In addition, for the PEM fuel cell stack of metallic BPP, the BPP exhibits larger manufacturing

* Corresponding author at: State Key Laboratory of Mechanical System and Vibration, Shanghai Jiao Tong University, School of Mechanical Engineering, 800 Dongchuan Road, Shanghai 200240, China. Tel.: +86 021 34206303; fax: +86 021 34204542.
E-mail addresses: daliu@sjtu.edu.cn (D. Liu), penglinfa@sjtu.edu.cn (L. Peng), xmlai@sjtu.edu.cn (X. Lai).

0378-7753/$ – see front matter © 2010 Elsevier B.V. All rights reserved.
doi:10.1016/j.jpowsour.2009.12.113

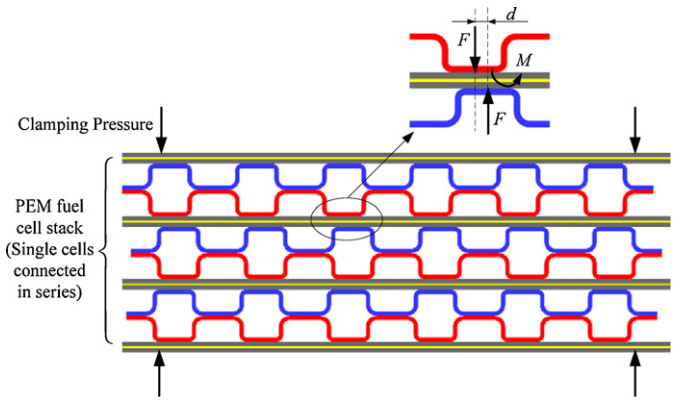

Fig. 1. Schematic of assembly error of metallic BPP in a PEM fuel cell stack.

error [15–17] because of its plastic characters (for example spring-back), which in turn makes the influence of assembly error more serious.

On one hand, the assembly error of BPP should be controlled and decreased in order to improve the performance of the PEM fuel cell stack. On the other hand, based on the current assembly process and manufacturing process, it is very hard to control the assembly error to a very low level. And moreover if the assembly error required is too small, the assembly and manufacturing cost of the PEM fuel cell stack will increase dramatically, which is unacceptable and conflict with the cost reduction of the PEM fuel cell. Therefore, there is a need to investigate the effect of the assembly error of the BPP on the contact behavior of PEM fuel cell stack in order to guide the assembly process, and furthermore obtain a tradeoff between the performance and the assembly accuracy.

Nevertheless, to the best of our knowledge, such researches have not been reported in literatures. There are only several studies about the influence of manufacturing and loading variations of the components in a PEM fuel cell stack released. Vlahinos et al. [18] first investigated the variations of material and manufacturing of the graphite BPP on the MEA pressure distribution. Zhang et al. [19] developed a FEA model for a PEM fuel cell and studied the effect of different load distributions on the contact resistance between the carbon-based BPP and GDL. Zhan et al. [20] studied the effect of porosity distribution variations on the liquid water flux through GDL with computation models. In one of our previous studies [21], the effect of assembly parameter variations on the GDL pressure distribution in a PEM fuel cell was investigated. A robust solution of the assembly parameters for the PEM fuel cell stack was obtained.

In this study, it is aimed to develop a methodology based on parameterized FEA model, LS-SVM simulation and statistical analysis to obtain the effect of the assembly error of the metallic BPP on the pressure distribution and stress failure of the MEA. A parameterized FEA model of a metallic BPP/MEA assembly is developed and the general rule of the effect of assembly error of BPP is obtained through the methodology described in this research.

2. Methodology

The main purpose of this study is to develop a methodology to obtain the effect of the assembly error of the BPP on the pressure distribution and stress failure of MEA. The schematic diagram of the methodology is shown in Fig. 2, which consists of the following three steps:

First, the well-established finite element method is employed for a parameterized FEA model of a two-cell metallic BPP/MEA assembly. Suitable meshing and material properties are assigned for the BPP and MEA. Loading conditions and contact behaviors are consistent with the actual physical situation. During the creation of the FEA model, the assembly position of each metallic BPP is fully parameterized, which can be updated based on the assembly error.

Then, based on the parameterized FEA model, the LS-SVM simulation process is developed. The assembly error of each metallic BPP is defined as the input variables, and the pressure distribution and maximum Von Mises stress of the MEA are selected as the output variables for the LS-SVM simulation. In order to build the LS-SVM model, the Latin hypercube sampling (LHS) method is employed to obtain the training sample and testing sample. After validating the prediction accuracy of the LS-SVM model, it can be used to analyze the effect of the assembly error.

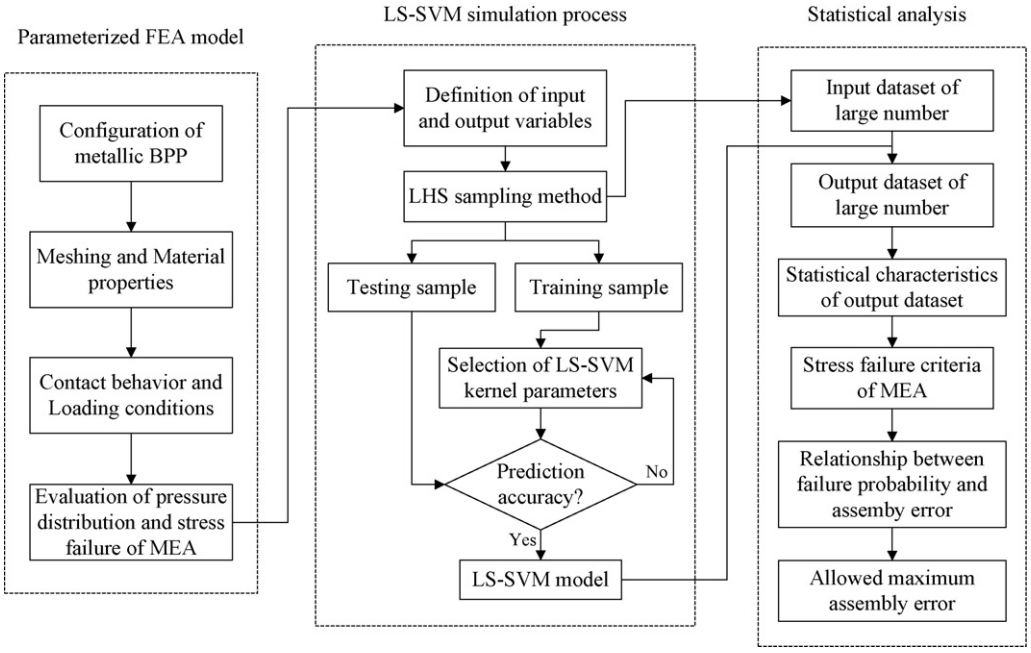

Fig. 2. Methodology for the effect of assembly error of BPP on pressure distribution and stress failure of MEA.

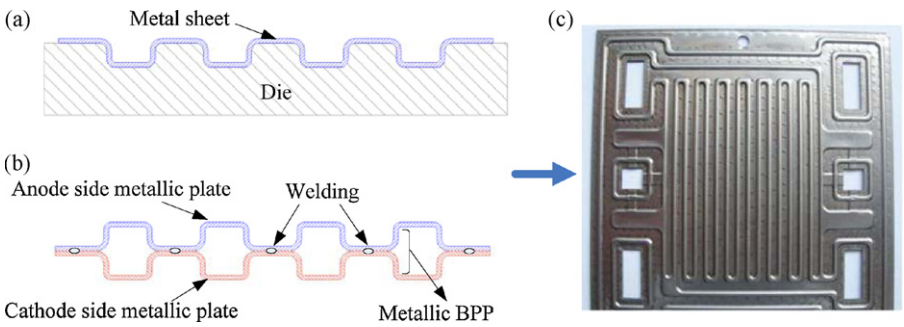

Fig. 3. (a) Single sided metallic plate based on forming process, (b) metallic BPP based on welding joining and (c) picture of joined metallic BPP for this research.

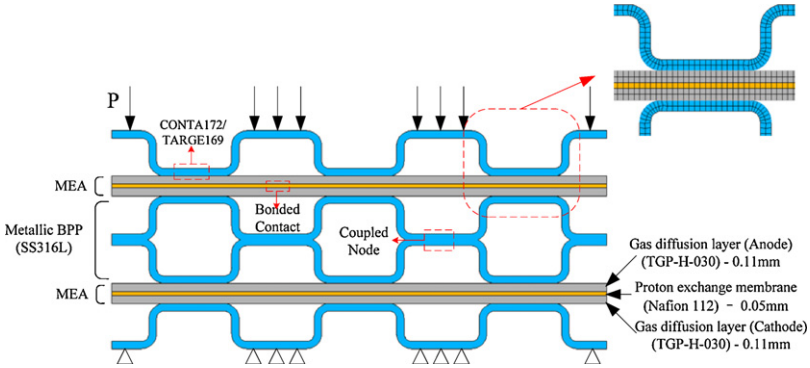

Fig. 4. Parameterized FEA model of a two-cell metallic BPP/MEA assembly.

Finally, a dataset for input variables of a large number (10,000) is generated with LHS sampling method again, which is input into the LS-SVM model obtained above. Then, with the LS-SVM model, a dataset of the output variables can be obtained. The statistical analysis is applied to the dataset of output variables to access the effect of the assembly error. At last, with the Von Mises stress failure criteria for the MEA, the relationship between the failure probability and the assembly error is obtained, and the allowed maximum assembly error is calculated based on the relationship equation as shown in Fig. 2.

3. Parameterized FEA model of metallic BPP/MEA assembly

According to the methodology in Section 2, a parameterized FEA model of a two-cell metallic BPP/MEA assembly stack is developed first. The commercial code of ANSYS is used to build the FEA model as follows.

3.1. Configuration of metallic BPP

The metallic BPP of this study is fabricated with metallic sheets based on the forming process (Fig. 3(c)). Considering the characteristics of the sheet forming process, one piece of metallic sheet can only be made into a single sided plate. This is because once one side of the metallic sheet is decided, the other side can not be changed because they are formed simultaneously (Fig. 3(a)).

However, in a PEM fuel cell, the BPP needs to provide H_2 on one side and air/O_2 on the other side simultaneously. Hence, two single sided plates are joined into one BPP by a welding process (for example spot welding) to fulfill the requirement of the PEM fuel cell in this study (Fig. 3(b)). With the metallic BPP obtained above, a two-cell BPP/MEA assembly model of three channels is developed as shown in Fig. 4.

3.2. Meshing and material properties

From Fig. 4, there are three main components in the FEA model, which are the GDL, proton exchange membrane (PEM) and metallic BPP. The generalized plane strain element PLANE82 of 8 nodes is chosen to represent the three components. A combination of mapped meshing and automatic meshing is employed in order to ensure the proper element connectivity and the correct aspect ratio as shown in Fig. 4.

The GDL of this study is Toray TGP-H-030 (0.11 mm in thickness) from Toray Industries, Inc., the PEM Nafion® 112 (0.05 mm in thickness), and the metallic BPP made of SS316L. Material properties of the GDL and the metallic BPP are listed in Table 1. Previous work [12] has shown that the mechanical response of the PEM is highly nonlinear and its stress failure is one of the key factors affecting the durability of the PEM fuel cell. Therefore, the elasto-plastic model with isotropic hardening and the Von Mises yield criteria are employed for the PEM in order to analyze its stress failure [11]. The corresponding data are listed in Tables 1 and 2.

Table 1
Material property for the components of the metallic BPP/MEA assembly.

Component	Material	Young's modulus (MPa)	Poisson's ratio	Bulk density ($g\,cm^{-3}$)
BPP	SS316	1.97e5	0.3	7.8
GDL	TGP-H-030	6.1	0.1	0.44
PEM	Nafion® 112	46 [13]	0.25	2

Table 2
Set of the hardening curve of Nafion® 112 [13].

True stress (MPa)	Plastic strain
2.2 (yield strength)	0
2.26	0.05
4.31	0.25

In the elasto-plastic model, the material behavior is divided into an elastic region and a plastic region. In the elastic region the Hooke's law is accepted. The constitutive law can be written as follows:

$$\sigma_{ij} = \frac{E}{(1+\nu)(1-2\nu)}(\nu\varepsilon_{ij}^{EL} + \sum_{k}(1-2\nu)\varepsilon_{kk}^{EL}\delta_{ij}) \quad (1)$$

where σ_{ij} is the stress tensor component, ν is the Poisson's ratio, E is the Young's modulus, and δ_{ij} is the Kroneker δ-symbol.In the plastic region, the plasticity behavior is described by Prandtl–Reuss theory and the Von Mises yield function is written as follows:

$$f(\sigma_{ij}) = \left(\frac{3}{2}S_{ij}S_{ij}\right)^{1/2} - \sigma_0 \quad (2)$$

where $\sigma_e = ((3/2)S_{ij}S_{ij})^{1/2}$ is the Von Mises stress and σ_0 the yield strength, and S_{ij} is the component of the deviatoric stress tensor. When $f(\sigma_{ij}) = 0$, the yield occurs for PEM based on Von Mises yield criterion. For $f(\sigma_{ij}) < 0$, the material deforms elastically.

3.3. Contact behavior and loading conditions

As shown in Fig. 4, there are three types of contact behaviors for the metallic BPP/MEA assembly, which are the contact between the BPP and the GDL, between the GDL and the PEM, and between the two single sided plates of the BPP. For each contact behavior, a different contact model is built based on its actual contact situation in this study (Fig. 4). For example, the traditional "surface to surface" contact model is created at the interface between the BPP and GDL with CONTA172 and TARGE169. For the interface between the PEM and GDL, the "bonded contact" (with no slip allowed) is defined because they are hot pressed together before assembled in the stack [3]. And, the "coupled node" contact behavior is developed between the two single sided plates because they are joined together by a welding process as shown in Fig. 3.

The FEA model has to be properly constrained in order to prevent the free movement. In this study, because the end plate is much thicker and more rigid than the BPP and MEA, it can be treated as a rigid body in the model to save the computing time. Thus, proper loading conditions are applied to simulate the assembly force instead of the end plate. Zero displacement of x-direction is applied at the left and right boundaries of the model, and zero displacement of y-direction condition is applied for the node on the bottom of the low BPP. The displacements for the nodes on the top of the up BPP are coupled in y-direction and a uniform clamping pressure $P = 2$ MPa is applied on these nodes to model the assembly pressure (Fig. 4) [12].

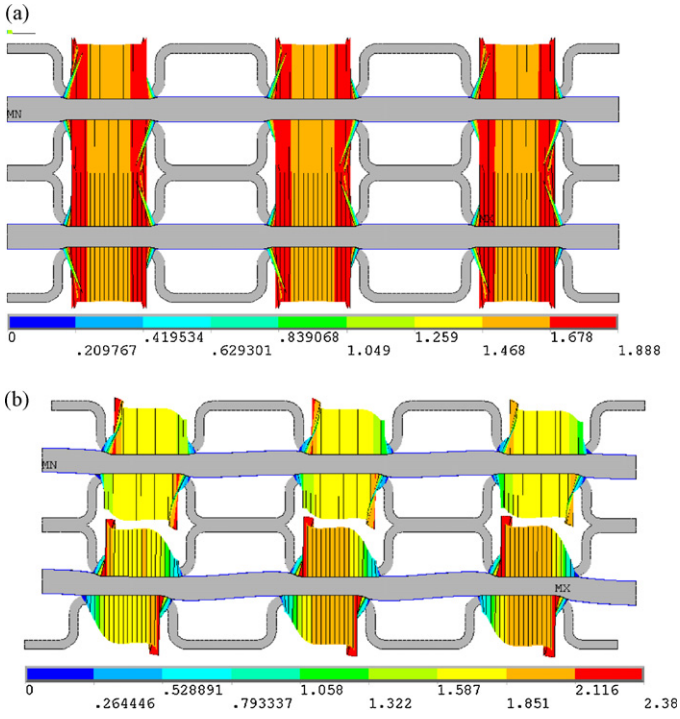

Fig. 5. Contact pressure distribution between BPP and MEA (a) without assembly error and (b) with assembly error.

3.4. Evaluation method of pressure distribution and stress failure of MEA

In this study, the mean μ_P and standard deviation σ_P of the pressure distribution, and the maximum Von Mises stress S_{max} of the MEA are used to evaluate its pressure distribution and stress failure, which can be obtained with the parameterized FEA model as follows:

$$\mu_P = \frac{\sum_{i=1}^{i=n} P_i}{n} \quad (3)$$

$$\sigma_P = \sqrt{\frac{1}{n}\sum_{i=1}^{i=n}(P_i - \mu_P)^2} \quad (4)$$

$$S_{max} = \mathrm{Max}(S_i) \quad (5)$$

where P_i is the contact pressure of each contact element on the MEA, n is the number of all the contact elements, and S_i is the Von Mises stress for each element of the PEM.

In this study, μ_P represents the average contact pressure and σ_P represents the uniformity of the contact pressure. When μ_P increases, it means that the contact behavior on the MEA becomes better. If σ_P increases, it means that the uniformity of pressure distribution becomes worse. S_{max} represents the stress concentration of the PEM and if S_{max} exceeds its yield strength, there will be residual stress in the PEM after unloading based on the Von Mises yield criteria, which in turn influences the durability of the PEM.

Fig. 5 illustrates the comparison of contact pressure distributions of the MEA with and without assembly error. As shown in Fig. 5, due to the assembly error of BPP, there is an assembly position deviation for the adjacent BPPs, which in turn makes the contact behavior non-uniform. According to Eqs. (3)–(5), for the BPP/MEA assembly without assembly error, μ_P, σ_P and S_{max} are 1.59, 0.29 and 1.89 MPa, respectively, while they are 1.64, 0.42 and 2.38 MPa for the assembly with assembly error. The difference between the two results shows the influence of the assembly error obviously.

4. LS-SVM simulation process for assembly error of BPP

The main purpose of this study is to analyze the effect of the assembly error of BPP on the contact pressure distribution and stress failure of the MEA, which, therefore, is a statistical problem. In this study, the LS-SVM simulation process is employed to conduct the analysis, because of its advantages and remarkable generalization performance [22].

In order to obtain the general rule for the effect of the assembly error, a range of assembly errors whose standard deviations are between 0.01 and 0.07 mm at interval of 0.01 mm are investigated with the methodology of this study. Thus, all together 7 LS-SVM simulations need to be conducted. Because of the similarity of each LS-SVM simulation, an arbitrary assembly error (for instance, whose standard deviation is 0.04 mm) is taken as an example to illustrate the simulation procedure of the LS-SVM in detail as follows.

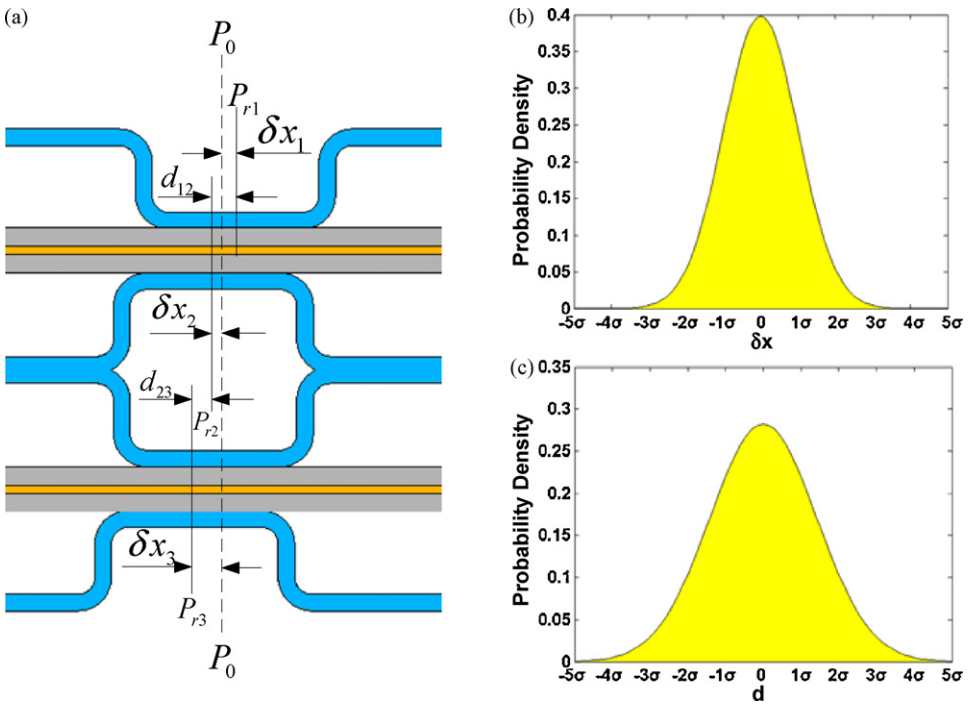

Fig. 6. Definition of assembly error of the metallic BPP.

4.1. Kernel function selection

When conducting the LS-SVM simulation, selection of the kernel function is a crucial problem need to be solved [23,24]. In principle, the LS-SVM always fits a linear relation ($y = \omega x + b$) between the regression x and the dependent variable y. The best relation is the one that minimizes the cost function J containing a penalized regression error term:

$$\begin{cases} \min J(\omega, e) = \dfrac{1}{2}\omega^T\omega + \gamma\dfrac{1}{2}\displaystyle\sum_{t=1} e_t^2 \\ s.t. \quad y_t = \omega^T\varphi(x_t) + b + e_t, \quad t = 1, \ldots, N \end{cases} \tag{6}$$

where $\varphi(x_t)$ denotes an infinite dimensional feature map.

By using the Lagrangian and partially differentiation method, the final resulting LS-SVM model can be evaluated at a new point x_* as:

$$\hat{f}(x_*) = \sum_{t=1}^{SV} \alpha_t K(x_*, x_t) + b \tag{7}$$

where SV is the number of support vectors (SVs) and $K(\cdot,\cdot)$ is kernel function, which must follow Mercer's theory.

There are several kernel functions for the LS-SVM simulation, such as linear, polynomial, radial basis function (RBF) kernel and multi-layer perceptron (MLP). In this work, the RBF kernel is selected as the kernel function (Eq. (8)) because it is a more compact supported kernel, and could reduce the computational complexity.

$$K(x, x_t) = \exp\left(\frac{-\|x - x_t\|^2}{\sigma^2}\right) \tag{8}$$

4.2. Definitions of input and output variables

For the LS-SVM simulation of this study, the output variables are the mean μ_P and standard deviation σ_P of the MEA pressure distribution, and the maximum Von Mises stress S_{max} of the PEM, which are determined by Eqs. (3)–(5). The input variables are the standard deviation of the assembly error of each BPP, which are defined by Eqs. (9)–(11) as follows:

As mentioned in Section 1, based on the current assembly process, the assembly error of the BPP is unavoidable, which leads to the assembly position deviation of the adjacent BPPs (Fig. 1). Hence, in this study, the difference between the nominal assembly position P_0 and the real assembly position P_r of each metallic BPP is defined as its assembly error (Fig. 6(a)).

$$\delta x = P_0 - P_r \tag{9}$$

According to the error theory and the large sample theory, the assembly error δx obeys the normal distribution as shown in Fig. 6(b) and Eq. (10):

$$\delta x \in N(0, \sigma) \tag{10}$$

where σ is the standard deviation for the assembly error δx of each BPP. Then, the assembly position deviation d of two adjacent BPPs can be defined as:

$$d_{ij} = \delta x_i - \delta x_j \in N(0, \sqrt{2}\sigma), \quad (|i - j| = 1) \tag{11}$$

where d is the main reason that causes the clamping force to transmit non-uniformly (Fig. 6(c)). From Eqs. (10) and (11), both δx and d are determined by σ, therefore, in this study σ is used to represent the assembly error δx of the BPP and taken as the input variable for the LS-SVM simulation.

4.3. Training sample and testing sample

In order to construct the LS-SVM simulation, there must be a proper training sample and testing sample for the input and output variables first. The Latin hypercube sampling (LHS) sampling method is employed to obtain the training sample and testing sample.

Fig. 7 shows the histogram of the training sample of the assembly error with its σ being 0.04 mm. As shown in Fig. 7, the assembly error accords with the normal distribution which is consistent with Eq. (10). Since its mean is 0 mm and standard deviation is 0.04 mm,

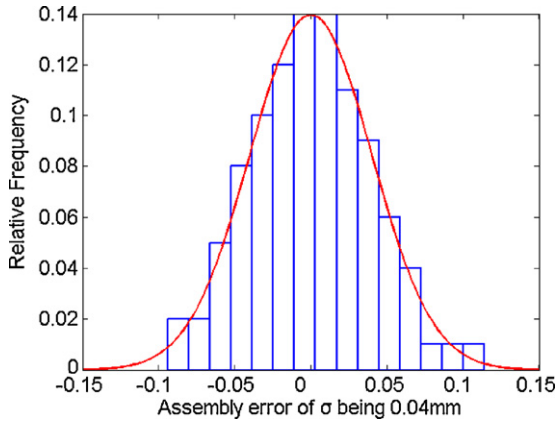

Fig. 7. Training sample of input variables for the assembly error with $\sigma = 0.04$ mm.

the assembly error is mainly between −0.12 and 0.12 mm according to the "Six Sigma" theory as shown in Fig. 7. Similarly, with LHS sampling method, the testing sample is also obtained for validating the LS-SVM model.

4.4. Parameter setting and prediction accuracy validation

Proper parameter setting plays a crucial role in building a LS-SVM simulation model with high prediction accuracy and stability. For the LS-SVM simulation model of this study, the RBF kernel function is employed (Eq. (8)), for which γ and σ^2 are two key parameters needing to be chosen carefully. In this work, the "grid search" technique and "leave one out cross validation" are employed to find the optimal parameter values, with values of γ and σ^2 in the range of 0.01–10,000. "Grid search" is a two-dimensional minimization procedure based on exhaustive search in a limited range. In each iteration, one leaves one point, and fits a model on the other data points. The performance of the model is estimated based on the points left out [24].

In order to validate the prediction accuracy of the LS-SVM, the results of the LS-SVM prediction and FEA model for the output variables are compared. Fig. 8 illustrates the comparison of the LS-SVM prediction and the FEA model for the output variable S_{max} with both training sample and testing sample, respectively. From Fig. 8, the prediction of the LS-SVM agrees well with the results of the FEA model, which indicates the high prediction accuracy of the obtained LS-SVM model. For the other two output variables μ_P and σ_P, the LS-SVM model also shows good prediction accuracy.

In order to further assess the prediction accuracy of the obtained LS-SVM model, the root mean square error of prediction (RMSEP) and the relative standard error of prediction (RSEP) for each output variable are obtained based on Eqs. (12) and (13) as listed in Table 3.

$$\text{RMSEP} = \sqrt{\frac{1}{n}\sum_{i=1}^{n}(\hat{y}_i - y_i)^2} \tag{12}$$

$$\text{RSEP}\ (\%) = 100 \times \sqrt{\frac{\sum_{i=1}^{n}(\hat{y}_i - \bar{y})^2}{\sum_{i=1}^{n}\hat{y}_i^2}} \tag{13}$$

Table 3
RMSEP and RSEP for the LS-SVM model.

Output variables	RMSEP	RSEP (%)
μ_P	0.0149	0.93
σ_P	0.0426	1.27
S_{max}	0.03	1.51

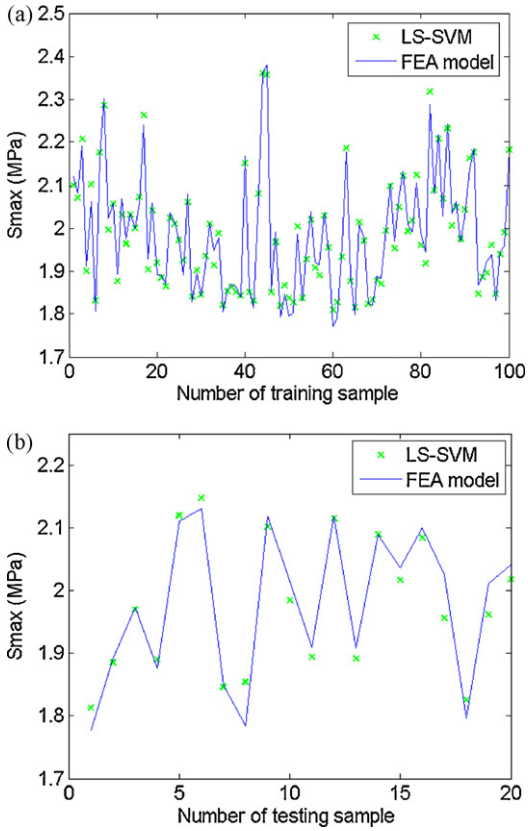

Fig. 8. Comparison of LS-SVM prediction and FEA model for S_{max} with (a) the training sample and (b) testing sample.

From Table 3, for each output variable, both RMSEP and RSEP (%) are at a very low value range (close to 0), which further indicates the obtained LS-SVM model of this study has a high prediction accuracy and can be used to further analyze the effect of the assembly error of BPP.

4.5. Statistical analysis of LS-SVM results

As mentioned above, the analysis of the assembly error is a statistical problem. Therefore, the statistical analysis is employed on LS-SVM simulation results to obtain the effect of the assembly error. The training sample and testing sample for the output variables obtained above are of small number (100 and 20, respectively), on which the statistical analysis cannot be conducted accurately.

Hence, with the LS-SVM model developed above, datasets of large number (10,000) for the output variables μ_P, σ_P and S_{max} are obtained to conduct the statistical analysis. Using LHS sampling method again, datasets of large number (10,000) for the input variables are obtained, which are then input into the LS-SVM model obtained above, and finally the corresponding datasets for the output variables of the same number (10,000) are obtained and the statistical analysis is conducted as shown in Fig. 9.

Fig. 9 presents the statistical analysis results of the output variables μ_P, σ_P and S_{max} of large number (10,000). As shown in Fig. 9, although the input variables are of normal distributions, the output parameters exhibit a certain degree of asymmetry of their distributions around their mean, especially for σ_P and S_{max}.

It also can be seen that the min and max of μ_P are 1.597 and 1.614 MPa, respectively, and it only increases by 1.1%, which is quite small. While σ_P increases by 56.8% (from 0.291 to 0.456 MPa), S_{max} increases by 41.4% (from 1.784 to 2.522 MPa). It means that this assembly error with its standard deviation σ being 0.04 mm has

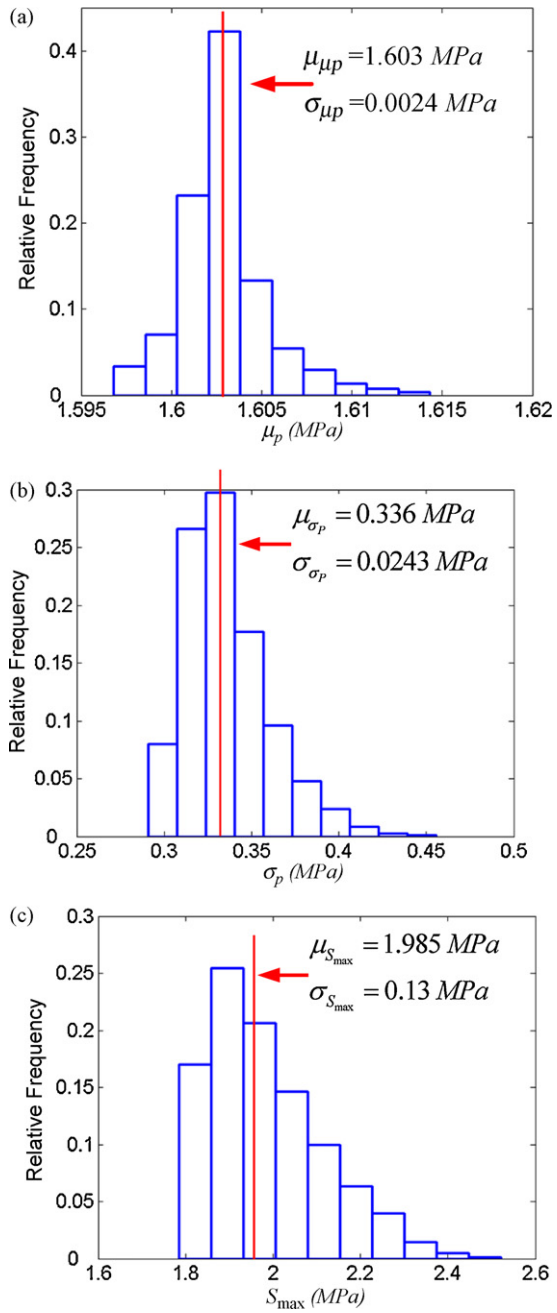

Fig. 9. Statistical analysis for (a) μ_P, (b) σ_P and (c) S_{max} of large number (10,000) for the assembly error with its σ being 0.04 mm.

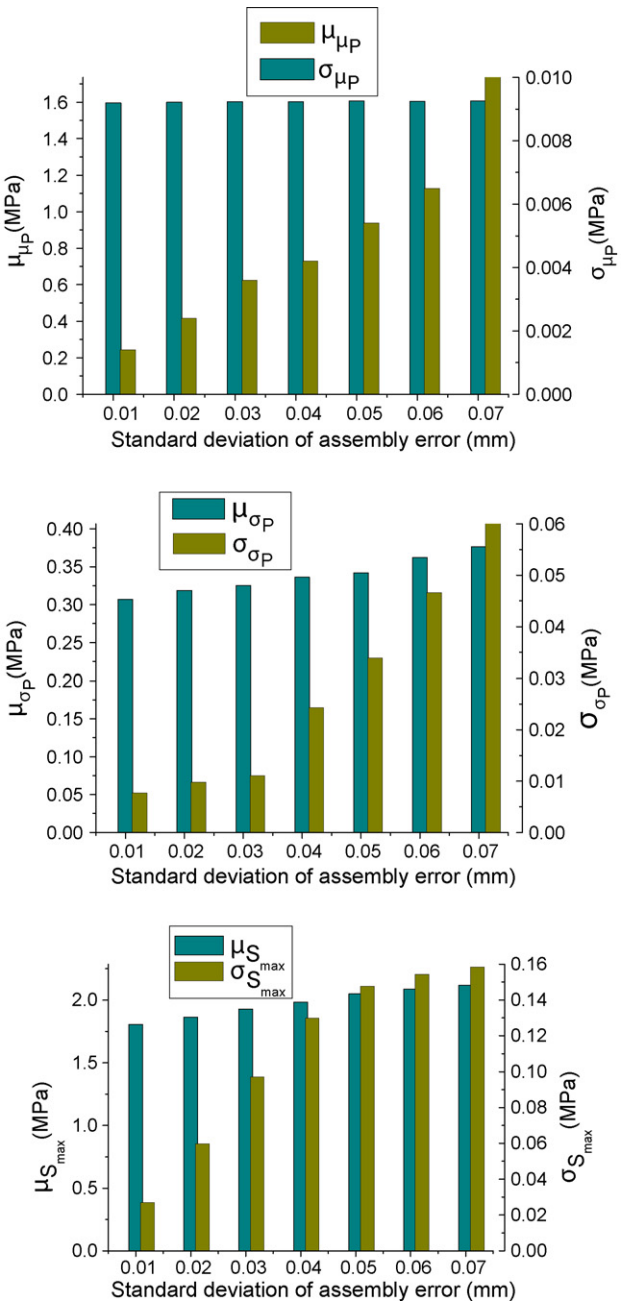

Fig. 10. Effect of assembly error on the statistical characteristics of (a) μ_P, (b) σ_P and (c) S_{max}.

more significant influence on the uniformity of the pressure distribution and stress concentration of the MEA. From Fig. 9(c), some values of the S_{max} are larger than the yield strength of 2.2 MPa (Table 2), which will result in plastic deformation and residual stress in PEM.

5. Results and discussion

The LS-SVM simulation process and statistical analysis are demonstrated in detail above with the assembly error whose standard deviation being 0.04 mm. Similarly, for the other 6 assembly errors, the LS-SVM simulations and the statistical analysis are also conducted using the same modeling process to obtain the general effect of the assembly error of the metallic BPP.

5.1. Effect on statistical characteristics of μ_P, σ_P and S_{max}

With the LS-SVM simulation process and the statistical analysis developed above, the statistical characteristics of μ_P, σ_P and S_{max} (i.e. μ_{μ_P}, σ_{μ_P}, μ_{σ_P}, σ_{σ_P}, $\mu_{S_{max}}$ and $\sigma_{S_{max}}$) for different assembly errors are obtained to assess the effect of the assembly error on the pressure distribution and stress failure of the MEA as shown in Fig. 10.

From Fig. 10(a), for the mean contact pressure μ_P on the MEA, its mean value μ_{μ_P} almost keeps the same (about 1.6 MPa), while its standard deviation σ_{μ_P} becomes larger with the increase of assembly error. However, the magnitude of σ_{μ_P} is quite smaller (<1%) than μ_{μ_P} for each assembly error. Hence, this means the mean contact pressure μ_P on MEA does not change much with the increase

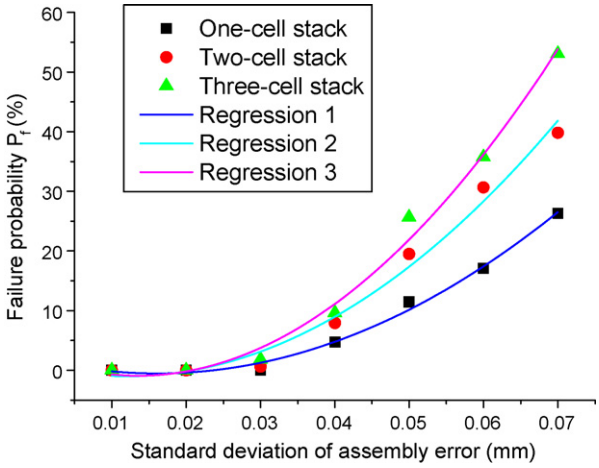

Fig. 11. Relationship between the failure probability P_f and the standard deviation of assembly error for three stacks.

of the assembly error, which is consistent with Fig. 9(a). This is mainly because the total clamping pressure P remains the constant of 2 MPa for the BPP/MEA assembly in this study, and therefore the total contact force on the interface keeps unchanged. Although the assembly error makes some contact at the interface become deeper, but at the same time the other part at the interface may have a shallower contact (Fig. 5(b)). Therefore, the assembly error has little effect on the mean contact pressure on the MEA.

From Fig. 10(b) and (c), for the pressure distribution uniformity σ_P and maximum Von Mises stress S_{max}, their mean values μ_{σ_P} and $\mu_{S_{max}}$ increase gradually with the increase of the assembly error. μ_{σ_P} increases by 23% (from 0.3 to 0.37 MPa), and $\mu_{S_{max}}$ increases by 17% (from 1.8 to 2.1 MPa). Furthermore, their standard deviations σ_{σ_P} and $\sigma_{S_{max}}$ increase rapidly as the assembly error increasing. This indicates the assembly error has a significant influence on the pressure distribution uniformity σ_P and maximum Von Mises stress S_{max} of the MEA. This is because the assembly position deviation of the adjacent metallic BPP becomes larger with the increase of the assembly error, which in turn makes the contact behavior between the BPP and MEA more non-uniform.

5.2. Effect on failure probability of PEM

As shown in Fig. 10(c), although all $\mu_{S_{max}}$ remain less than the yield strength of 2.2 MPa, some of S_{max} may exceed 2.2 MPa due to the influence of $\sigma_{S_{max}}$, which in turn causes the PEM to deform plastically and do harm to its durability.

As mentioned in Section 1, the plastic deformation of the PEM causes residual stress after unloading, which affects the stress failure of the PEM [11–14]. Therefore, in this study a relatively higher failure criterion ($S_{max} > 2.2$ MPa) is used as a measurement of the PEM failure based on Von Mises yield criteria (Eq. (2)), and the probability of $S_{max} > 2.2$ MPa for each assembly error is defined as its failure probability P_f . Based on the dataset for S_{max} of large number (10,000) obtained with LS-SVM simulation developed above, the number N_f of $S_{max} > 2.2$ MPa for each assembly error is obtained. Then, the failure probability P_f is calculated as $P_f = N_f/10,000$.

Fig. 11 shows the relationship between the failure probability P_f and the assembly error. From Fig. 11, the failure probability increases quickly as the assembly error increasing, especially when the assembly error is in a large value range. Since the failure probability represents the durability of the PEM, this means that the PEM durability become worse with the increase of the assembly error.

In addition, in this study two other PEM fuel cell stack configurations (i.e. one-cell stack and three-cell stack) are also developed to investigate the effect of the number of BPP on the failure probability of the PEM. The failure probability P_f for the one-cell stack and three-cell stack are also plotted in Fig. 11. As shown in Fig. 11, the failure probability P_f for the three stack configurations presents the same trend with the increase of the assembly error, which indicates the robustness of the methodology of this study. More importantly, the failure probability P_f increases as the number of BPP increasing under the same assembly error (i.e. three-cell > two-cell > one-cell), which means there exists an error accumulation between the BPPs.

Regression equations between the failure probability P_f and the standard deviation σ of the assembly error are modeled using the

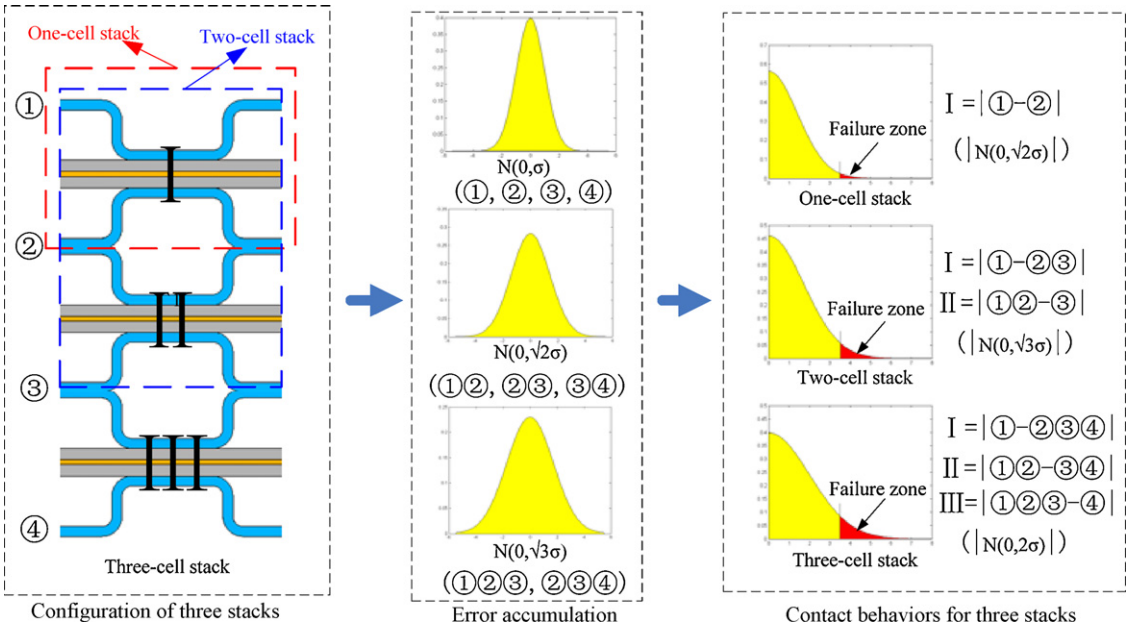

Fig. 12. Basic mechanism of error accumulation between adjacent BPPs for three stack configurations.

least squares (LS) method for each PEM fuel cell stack configuration to obtain the general rule as shown in Fig. 11 and Eq. (14).

$$\begin{cases} P_{f\_one} = 0.0192 - 3.023\sigma + 93.44\sigma^2 \\ P_{f\_two} = 0.00841 - 3.063\sigma + 127.441\sigma^2 \\ P_{f\_three} = 0.0225 - 4.654\sigma + 171.798\sigma^2 \end{cases} \quad (14)$$

where P_{f_one}, P_{f_two} and P_{f_three} are the failure probability for one-cell stack, two-cell stack and three-cell stack, respectively, and σ is the standard deviation of the assembly error.

Considering the current assembly process and taking a relative larger value of 10% as the allowed maximum failure probability, the allowed maximum standard deviations of the assembly error are then calculated as 0.05 mm for one-cell stack, 0.04 mm for two-cell stack and 0.037 mm for three-cell stack, respectively based on Eq. (14). Therefore, according to the "Six Sigma" theory, the allowed maximum assembly tolerances are 0 ± 0.15, 0 ± 0.12 and 0 ± 0.111 mm for the three PEM fuel cell stack configurations, respectively.

Both Fig. 11 and the calculated allowed maximum assembly errors for each PEM fuel cell stack configuration indicate that the effect of the assembly error becomes more serious with the increase of the number of BPP. This means there exits an error accumulation between the BPPs in the PEM fuel cell stack, which can be explained with Fig. 12.

As shown in Fig. 12(a), for the three stack configurations, there are three different contact pairs (i.e. I, II and III). These contact pairs are influenced by the assembly position deviation of the adjacent BPPs, which are different based on the stack configurations. For example, the contact pair "I" which is determined by BPPs "① " and "② " in the one-cell stack, while by BPPs "① " and "② ③ " in the two-cell stack and by BPPs "① " and "② ③ ④ " in the three-cell stack, respectively.

From Fig. 12(b), assuming the assembly error of each metallic BPP (①, ②, ③ and ④) of the same distribution of $N(0, \sigma)$, the assembly errors for the two and three adjacent BPPs then accord with the distribution of $N(0, \sqrt{2}\sigma)$ and $N(0, \sqrt{3}\sigma)$, respectively based on Eq. (11). Hence, the distribution fluctuation of the same contact pair becomes worse as the number of BPPs increasing under the same assembly error. This explains why the failure probability P_f increases as the number of the BPP increasing and the mechanism of the error accumulation of the adjacent BPPs (Fig. 12(c)).

Taking a certain value (for instance 3.5σ) as the critical failure standard for each stack configuration, then, the failure zone increases as the BPPs number increasing because of the error accumulation as shown in Fig. 12(c), which is consistent with Fig. 11.

In a real PEM fuel cell stack, because of the nonlinear contact and especially the plastic material property, the assembly error accumulation is more complicated and nonlinear. However, Fig. 12 explains the basic mechanism of the assembly error accumulation of adjacent BPPs in a PEM fuel cell stack, which is helpful for the design of the assembly process.

6. Conclusion

In this study, a methodology based on parameterized FEA model, LS-SVM simulation and statistical analysis is developed to investigate the effect of the assembly error of the metallic BPP on the pressure distribution and stress failure of MEA. It is demonstrated that the proposed numerical simulation scheme is feasible and effective for the assembly error considered.

From the results of this research, it can be seen that because of the assembly error of the BPP, both the pressure distribution and stress failure of MEA exhibit a certain degree of asymmetry of their distribution around their mean. With the increase of the assembly error, it has a significant effect on the uniformity of the pressure distribution σ_P and maximum Von Mises stress S_{max} of the MEA (increasing by 23% and 17%, respectively), while has little effect on the mean contact pressure μ_P.

The relationship between the failure probability P_f and the standard deviation σ of assembly error is obtained for three different stack configurations, which indicates that the failure probability P_f increases quickly with the increase of the assembly error for all three stacks, especially when the assembly error is in a large value range. According to the regression equations, the allowed maximum standard deviations of the assembly error are calculated as 0.05, 0.04 and 0.037 mm for the three stack configurations, respectively. And the allowed maximum assembly tolerances for the three stack configuration are then obtained as 0 ± 0.15, 0 ± 0.12 and 0 ± 0.111 mm based on the "Six Sigma" theory.

It is found that there exists an assembly error accumulation for the adjacent BPPs in the PEM fuel cell stack, which is the main reason that the failure probability increases as the number of the BPPs increasing in a stack. The basic mechanism of this assembly error accumulation is also revealed by this research. The conclusion and methodology developed in this study are beneficial in improving the assembly accuracy and can be applied to guide the assembly process for the PEM fuel cell stack.

Acknowledgements

This work is supported by National Natural Science Foundation of China (No. 50805092), Major International (Regional) Joint Research Project (No. 50820125506) and the Program of Introducing Talents of Discipline to Universities (No. B06012). The authors are gratefully acknowledged for their supports.

References

[1] G. Hoogers, Fuel Cell Technology Handbook, CRC Press, Boca Raton, FL, 2003.
[2] P. Zhou, C.W. Wu, G.J. Ma, Journal of Power Sources 159 (2006) 1115–1122.
[3] Y. Zhou, G. Lin, A.J. Shih, S.J. Hu, Journal of Power Sources 192 (2009) 544–551.
[4] V. Mishra, F. Yang, R. Pitchumani, Journal of Fuel Cell Science and Technology 1 (2004) 2–9.
[5] S.-J. Lee, C.-D. Hsu, C.-H. Huang, Journal of Power Sources 145 (2005) 353–361.
[6] W.-K. Lee, C.-H. Ho, J.W. Van Zee, M. Murthy, Journal of Power Sources 84 (1999) 45–51.
[7] C.-Y. Wen, Y.-S. Lin, C.-H. Lu, Journal of Power Sources 192 (2009) 475–485.
[8] P. Zhou, C.W. Wu, G.J. Ma, Journal of Power Sources 163 (2007) 874–881.
[9] D. Bograchev, M. Gueguen, J.-C. Grandidier, S. Martemianov, International Journal of Hydrogen Energy 33 (2008) 5703–5717.
[10] Y. Tang, A. Kusoglu, A.M. Karlsson, M.H. Santare, S. Cleghorn, W.B. Johnson, Journal of Power Sources 175 (2008) 817–825.
[11] D. Bograchev, M. Gueguen, J.-C. Grandidier, S. Martemianov, Journal of Power Sources 180 (2008) 393–401.
[12] A. Kusoglu, A.M. Karlsson, M.H. Santare, S. Cleghorn, W.B. Johnson, Journal of Power Sources 161 (2006) 987–996.
[13] A. Kusoglu, A.M. Karlsson, M.H. Santare, S. Cleghorn, W.B. Johnson, Journal of Power Sources 170 (2007) 345–358.
[14] Y. Tang, A.M. Karlsson, M.H. Santare, M. Gilbert, S. Cleghorn, W.B. Johnson, Materials Science and Engineering A 425 (2006) 297–304.
[15] M. Koç, S. Mahabunphachai, Journal of Power Sources 172 (2007) 725–733.
[16] D.A. Liu, L. Peng, X. Lai, International Journal of Hydrogen Energy 34 (2009) 990–997.
[17] T. Matsuura, M. Kato, M. Hori, Journal of Power Sources 161 (2006) 74–78.
[18] A. Vlahinos, K. Kelly, J. D'Aleo, J. Stathopoulos, First International Conference on Fuel cell Science Engineering and Technology, Rochester, New York, USA, April 21–23, 2003.
[19] L. Zhang, Y. Liu, H. Song, S. Wang, Y. Zhou, S.J. Hu, Journal of Power Sources 162 (2006) 1165–1171.
[20] Z. Zhan, J. Xiao, D. Li, M. Pan, R. Yuan, Journal of Power Sources 160 (2006) 1041–1048.
[21] D.A. Liu, X. Lai, J. Ni, L. Peng, S. Lan, Z. Lin, Journal of Power Sources 172 (2007) 760–767.
[22] T. Sun, H. Lin, H. Xu, Y. Ying, Postharvest Biology and Technology 51 (2009) 86–90.
[23] A. Niazi, S. Sharifi, E. Amjadi, Journal of Electroanalytical Chemistry 623 (2008) 86–92.
[24] D. Wu, Y. He, S. Feng, D.-W. Sun, Journal of Food Engineering 84 (2008) 124–131.